THE ASTROPHYSICAL JOURNAL, 497:404–418, 1998 April 10
© 1998. The American Astronomical Society. All rights reserved. Printed in U.S.A.

OPTICAL AND NEAR-INFRARED MODEL IMAGES OF THE CIRCUMSTELLAR ENVIRONMENTS OF CLASSICAL T TAURI STARS

KENNETH WOOD,[1] SCOTT J. KENYON,[1] BARBARA WHITNEY,[2] AND MARGARET TURNBULL[3]
Received 1997 June 6; accepted 1997 November 14

ABSTRACT

We describe model calculations of optical and near-infrared scattered light images expected from class II T Tauri stars—the star-plus-disk systems. The parameters controlling the disk shape, size, and mass are chosen to be within theoretically and observationally derived limits. We restrict our models to nearly edge-on disks, since for lower inclinations the central starlight is many orders of magnitude greater than the radiation scattered in the disk. In addition to model flux images, we calculate spectral energy distributions for pole-on viewing using approximations for flat and flared disks. We find that direct imaging of edge-on disks can provide only estimates of the scale height at large distances from the central star and an estimate of the disk mass. The images are rather insensitive to the inner disk radius and the degree of flaring, provided the scale height is fixed at large radii. Spectral energy distribution modeling is required to constrain the inner disk radius and the degree of flaring.

We apply our models to recent *Hubble Space Telescope* (*HST*) images of HH 30 IRS and investigate whether the scattered light images could have been produced by starlight scattering off the walls of jet-carved cavities in infalling envelopes associated with the embedded class I sources. We find that while the class I infalling envelope plus cavity model qualitatively resembles the *HST* images, the spatial extent of the model images is too large. Edge-on disk models appear to provide better fits to the data and enable us to determine the disk scale height at large distances from the central star. However, the assumption of axisymmetry and uniform illumination is clearly inadequate for this variable source. In addition to producing flux images, our radiation-transfer simulations predict the spatially resolved polarization structure of HH 30. We have also performed *K*-band simulations for HH 30 in anticipation of high-resolution infrared imaging polarimetry.

Subject headings: circumstellar matter — radiative transfer — stars: individual (HH 30) — stars: pre–main-sequence

1. INTRODUCTION

Recent high spatial, spectral, and temporal resolution ground- and space-based observations have clearly demonstrated the nonsphericity of the circumstellar environments of T Tauri stars (Chandler et al. 1995; Stapelfeldt et al. 1995; Burrows et al. 1996). Much theoretical effort has been devoted to developing a coherent picture for the formation of these low-mass stars. The standard picture envisages the collapse of a self-gravitating protostellar cloud to form a star plus accretion disk system (see, e.g., Shu, Adams, & Lizano 1987). This collapse is followed by a longer phase during which the infalling cloud and disk are dispersed, either by accretion onto the central star or in strong outflows, leaving a naked T Tauri star. These phases of star formation are separated into three broad categories. Class I sources are heavily extincted stars whose optical and near-infrared (near-IR) light is scattered off the walls of cavities carved by outflows in their natal dust clouds (Whitney & Hartmann 1993; Kenyon, Calvet, & Hartman 1993a, Kenyon et al. 1993b; Whitney, Kenyon, & Gomez 1997; Lucas & Roche 1997). The class II, optically visible, classical T Tauri stars are the star-plus-disk systems that exhibit large IR and UV excesses compared to a stellar photosphere (Cohen & Kuhi 1979; Lada 1987). These sources are often highly variable on timescales of hours to weeks (see, e.g., Herbst, Herbst, & Grossman 1994). Once the circumstellar material has been either accreted or dispersed, a naked, slowly rotating, class III T Tauri star is left.

Theoretical investigations into the earliest, class I, phase have predicted the geometry of the infalling cloud (Ulrich 1976; Shu 1977; Cassen & Moosman 1981; Terebey, Shu, & Cassen 1984). Including cavities in these infalling clouds has enabled the modeling of scattered light images of such sources (Whitney & Hartmann 1993; Kenyon et al. 1993a, 1993b; Fischer, Henning, & Yorke 1994, 1996; Whitney et al. 1997; Lucas & Roche 1997). The spectral energy distributions of class II sources are commonly explained via dust emission from accretion disks, where the disk luminosity is caused by a combination of reprocessed stellar radiation and accretion luminosity (Adams & Shu 1986; Adams, Lada, & Shu 1987; Kenyon & Hartmann 1987). Recently the "magnetic accretion" model (Ghosh & Lamb 1979a, 1979b; Konigl 1991; Ostriker & Shu 1995, and references therein) has been applied to explain other observational properties of class II sources. In this model, disk material is accreted along magnetic field lines onto the poles of a dipole stellar magnetic field that may not be aligned with the stellar rotation axis. As the material falls onto the star, it forms bright rings or spots on the stellar surface. These spots rotate with the star and produce periodic or quasi-periodic modulations in the UV excess emission (Bouvier & Bertout 1989; Bouvier et al. 1993; Mahdavi & Kenyon 1998). This model can also explain the IR spectral energy distributions of many T Tauri stars (Bertout, Basri,

[1] Smithsonian Astrophysical Observatory, 60 Garden Street, Cambridge, MA 02138; kenny@claymore.harvard.edu; kenyon@payne.harvard.edu.
[2] Wisconsin Small Business Development Center, 432 North Lake Street, Madison, WI 53706; bwhitney@facstaff.wisc.edu.
[3] Department of Astronomy, University of Wisconsin, 475 North Charter Street, Madison, WI 53706; turnbull@uwast.astro.wisc.edu.

& Bouvier 1988; Kenyon, Yi, & Hartmann 1996) and may resolve the problem of low rotational velocities among classical T Tauri stars (Bouvier et al. 1993; Edwards et al. 1993).

Optical and near-IR images of T Tauri stars reveal direct stellar radiation and scattered radiation from their extended circumstellar environments. Whitney & Hartmann (1992, 1993) showed that, for class II sources viewed at low inclinations, the direct starlight would swamp the scattered radiation from the disk. Thus it would be possible, using standard techniques, only to image highly inclined class II sources (where the central star is occulted by the disk) or class I sources where the stellar radiation reaches us via scattering off the walls of cavities in their infalling envelopes. Radiation-transfer modeling of T Tauri stars using axisymmetric disks, envelopes, and bipolar cavities has been fairly successful in reproducing the observed scattered light images and spectral energy distributions (Whitney & Hartmann 1993; Kenyon et al. 1993a, 1993b). However, recent efforts to model polarimetric images suggest that fully three-dimensional models are required (Whitney et al. 1997; Lucas & Roche 1997). Near-IR images indicate patchy extinction in some sources (see, e.g., Chandler et al. 1995; Whitney et al. 1997). Some sources also show evidence for multiple jet events, deflected jets, or single jets with a variable ejection axis (see, e.g., Bally et al. 1995; Gomez, Kenyon, & Whitney 1998; Whitney et al. 1997). Although ground-based polarimetric imaging indicates the need for multiple cavities, it is only with high spatial resolution imaging that we may resolve these cavities and determine their morphologies.

This paper describes radiation-transfer simulations that examine the diffuse structures that are formed through the scattering of radiation in the circumstellar environments of optically visible, classical T Tauri stars—the class II star-plus-disk systems. Since previous investigations have shown that the disks will be visible only in scattered light at high inclinations, we restrict the model image presentation to nearly edge-on systems. In addition, we fix the disk parameters—scale height, degree of flaring, and density—within the limits set by theoretical models for optically thick accretion disks (Shakura & Sunyaev 1974; Kenyon & Hartmann 1987). Our models, presented in § 4, show that images can constrain the disk scale height at large radii and provide an estimate of the total disk mass. While the model images are insensitive to the degree of flaring and the location of the inner radius of the disk, the resulting spectral energy distributions *are* sensitive to these parameters.

The recent high-resolution images of HL Tau (Stapelfeldt et al. 1995; Close et al. 1997) and HH 30 (Burrows et al. 1996) are two examples of scattered light imaging of the circumstellar environments of young stellar objects. The scattered light pattern for HL Tau displays the characteristics of a class I source viewed at intermediate inclination, whereby light is seen from scattering in bipolar cavities within the protostellar cloud. In the case of HH 30, Burrows et al. modeled the circumstellar environment with a flared disk geometry viewed almost edge-on. The large flaring of the Burrows et al. disk mimics a cavity within an infalling circumstellar envelope, which motivated us to investigate whether HH 30 could be modeled as a class I source (§ 5.1.1 below). We also reexamined the disk geometry but limited our model parameters by theoretical and observational constraints (§ 5.1.2). Our Monte Carlo radiation-transfer models include emission from a central star plus jet and multiple scattering in the dusty circumstellar environment, yielding predictions of the spatially resolved flux and polarization at optical and near-IR wavelengths. Our analysis enables us to place limits on the scale height and mass of the disk surrounding HH 30.

Section 2 presents the adopted disk geometry for our simulations and an overview of the theoretical and observationally derived limits on the parameters controlling the disk. Section 3 outlines the radiation-transfer techniques and the adopted dust properties. Section 4 presents the results of our Monte Carlo radiation-transfer simulations of various disk masses and geometries, and the HH 30 investigation is presented in § 5. We conclude with a discussion of our findings and of what parameters can reasonably be obtained from the modeling of scattered light images of T Tauri disks.

2. CIRCUMSTELLAR DISK STRUCTURE

For the models in this paper, we adopt a disk structure in which the total density (gas plus dust) in the cylindrical (ϖ, z) coordinate system is

$$\rho = \rho_0 (\varpi / R_*)^{-\alpha} e^{-1/2[|z|/h(\varpi)]^2} , \quad (1)$$

where ρ_0 is the midplane density at $\varpi = R_*$ and α controls the radial variation of the density. We assume that the gas and dust are well mixed throughout a disk in vertical hydrostatic equilibrium (Shakura & Sunyaev 1973). The disk scale height, $h(\varpi)$, is

$$h(\varpi) = h_0 \left(\frac{\varpi}{R_*} \right)^{\beta} , \quad (2)$$

where h_0 is the scale height of the disk at the stellar surface, R_*. The mass of the disk is then

$$M_{\rm disk} = (2\pi)^{3/2} \frac{\rho_0 h_0 R_*^{\alpha-\beta}}{\beta - \alpha + 2} (R_{\rm max}^{\beta-\alpha+2} - R_{\rm min}^{\beta-\alpha+2}) . \quad (3)$$

As shown by Shakura & Sunyaev (1973), the disk scale height varies with radius according to

$$h = \left(\frac{c^2 \varpi^3}{G M_*} \right)^{1/2} . \quad (4)$$

The sound speed is $c^2 = kT/m$, where m is the mass of a dust particle. Assuming that the temperature follows a power law with radius, $T \propto \varpi^{-q}$, then the scale height varies as $h \propto \varpi^{(3-q)/2}$. Within the first few stellar radii, the disk temperature falls as $1/\varpi$ for flat and flared disks; at large radii, a flat disk asymptotes to $q = \frac{3}{4}$, while flared disks approach $q = \frac{1}{2}$ (Adams et al. 1987; Kenyon & Hartmann 1987). Thus the flaring will be in the range $9/8 \leq \beta \leq 5/4$ for centrally heated disks in which the gas and dust are well mixed. Disks could be heated by accretion luminosity and for steady accretion disks $T \propto \varpi^{-3/4}$, again giving $\beta = 9/8$ (Lynden-Bell & Pringle 1974). Without invoking time-dependent accretion or external heating (e.g., by a remnant protostellar envelope; D'Alessio, Calvet, & Hartmann 1997), it is difficult to make the disk temperature structure fall more slowly than $\varpi^{-1/2}$, thus making $\beta = 5/4$ an upper limit to the flaring. Indeed, the observational limits on β, from observations of the slope of the IR spectral energy distributions of classical T Tauri stars, suggest that the flaring is within these limits (Kenyon & Hartmann 1987, 1995). An isother-

mal disk, $\beta = 3/2$, appears to be ruled out by the observations.

Disk radii are on the order of a few hundred AU (see, e.g., Beckwith et al. 1990; Osterloh & Beckwith 1995; Dutrey et al. 1996). These sizes are inferred from the wavelength of the turnover of the far-IR spectral energy distribution, at which point the disk is optically thin, or from interferometric imaging. The inner radius of the disk is set either by the dust destruction radius or the radius at which magnetic pressure disrupts the disk in the magnetic accretion models (Lada & Adams 1992; Kenyon, Yi, & Hartmann 1996). Inner disk radii are typically several stellar radii; this estimate is supported by the observed near-IR excesses (Hillenbrand et al. 1992; Lada & Adams 1992; Kenyon, Yi, & Hartmann 1996; Meyer, Calvet, & Hillenbrand 1997). These inner disk "holes" may be physical holes or "opacity holes," whereby the dust is destroyed, but still leaving a smaller gas opacity. Too large a hole in the disk will not allow for dust at high enough temperatures to produce the observed near-IR emission. Disk masses are usually inferred from millimeter-continuum observations, which indicate masses in the range $0.001\ M_\odot \leq M_{\rm disk} \leq 0.1\ M_\odot$ (Beckwith et al. 1990; Adams, Emerson, & Fuller 1990; Osterloh & Beckwith 1995).

3. RADIATION-TRANSFER TECHNIQUES

We construct model images with a Monte Carlo radiation-transfer code that accounts for multiple photon scattering and predicts the spatially resolved flux and polarization (Whitney & Hartmann 1992, 1993; Wood et al. 1996a, 1996b, 1996c; Whitney et al. 1997). We assume that all radiation is stellar in origin. At the optical and near-IR wavelengths we simulate, this assumption is reasonable. The inner regions of the disk will contribute some near-IR emission (see Fischer, Henning, & Yorke 1994), but, as is evident in our spectral energy distribution calculations, this will be very small because of the inner disk hole. In the radiation-transfer calculation, the dust and gas mixture has albedo a, scattering polarization p, and a scattering phase function that is approximated by the Henyey-Greenstein phase function (Henyey & Greenstein 1941) with the asymmetry parameter g. For isotropic scattering, $g = 0$, while for completely forward scattering, $g = 1$. We choose to model the disk opacity using a Kim, Martin, & Hendry (1994) grain mixture and the appropriate scattering and polarization properties (a, g, and p). The adopted parameters are presented in Table 1. The opacities and scattering parameters are for the total gas plus dust mixture. The Kim et al. (1994) mixture reproduces many of the observed properties of interstellar dust. We thus assume that the circumstellar dust has the same optical properties as interstellar dust. Whitney et al. (1997) showed that the Kim et al. (1994) grain mixture successfully reproduces the colors of class I sources in Taurus; however, it tends to underestimate the polarization of the Taurus protostars. We keep the dust parameters fixed throughout our simulations.

TABLE 1

DUST PARAMETERS

Band	κ	a	g	p
R	160	0.50	0.40	0.47
I	110	0.50	0.36	0.55
K	22	0.35	0.25	0.60

We calculate the emergent spectral energy distribution from the star-plus-disk system using the approximations for the reprocessing of stellar radiation in flat and flared disks described by Kenyon & Hartmann (1987) and Adams & Shu (1986). For the flared disk geometry, Kenyon & Hartmann (1987) assumed that radiation from the star was absorbed at the point where the stellar photons impact the surface of a flared disk, which was chosen to lie at 3 scale heights above the midplane. They then assumed that the absorbed stellar radiation heats the disk midplane at the point directly below where the stellar photons were absorbed on the disk surface. Assuming that the disk midplane then radiates as a blackbody, with a radial temperature profile derived from the stellar heating, the resulting spectral energy distribution may be calculated. This approximation assumes that all stellar photons that hit the disk surface are absorbed and does not account for scattering or the possibility of photons penetrating deeper into the disk before being absorbed or scattered. This method therefore overestimates the disk flux and provides an upper limit to the amount of disk emission from reprocessed stellar radiation. For flat disks, we use the Adams & Shu (1986) analysis for reprocessing stellar radiation in an optically thick planar disk, which will intercept and reradiate one quarter of the stellar luminosity. The actual spectral energy distribution arising from reprocessing stellar radiation in a flared disk is likely to lie between the limits set by these two approximate methods of calculation.

4. MODEL IMAGES

The I- and K-band model images described in this section are for disk geometries specified by equations (1) and (2) with the following parameters (Table 2). The disk flaring is in the range $9/8 \leq \beta \leq 3/2$; scale heights at 100 AU are 7 AU, 15 AU, and 30 AU; disk masses are in the range $10^{-5}\ M_\odot \leq M_{\rm disk} \leq 10^{-2}\ M_\odot$, which translate into I-band equatorial optical depths in the range $10^4 \leq \tau_{\rm eq}(I) \leq 10^6$. We assume a stellar radius of 2 $R_\odot$, inner and outer disk radii of $3R_*$ and 250 AU, respectively, and a radial density exponent of $\alpha = 2$. Figures 1*a*, 2*a*, and 3*a* show the model images. The model images have been convolved with a Voigt profile of FWHM of 30 AU ($\sim 0.2''$ assuming a distance to Taurus of 140 pc) that is comparable to the *HST* point-spread function. We have not shown the polarization maps for these images since they are similar to those presented by Whitney & Hartmann (1992). However, we do show the predicted polarization pattern for our HH 30 investigation in § 5. In addition to these Monte Carlo simulations, we also present calculations of the pole-on spectral energy distributions (Figs. 1*b*, 2*b*, and 3*b*) using the Kenyon & Hartmann (1987) technique for flared disks and the Adams & Shu (1986) analysis for flat disks.

TABLE 2

MODEL PARAMETERS

Parameter	Value
β	9/8, 6/5, 3/2
H(100 AU) (AU).....	7, 15, 30
R_* ($R_\odot$)	2
$R_{\rm in}$ (R_*).....	3
$R_{\rm disk}$ (AU)	250
$M_{\rm disk}$ ($M_\odot$)	10^{-5} to 10^{-2}
$\tau_{\rm eq}(I)$ ($M_\odot$)	10^4–10^6
α.....	2

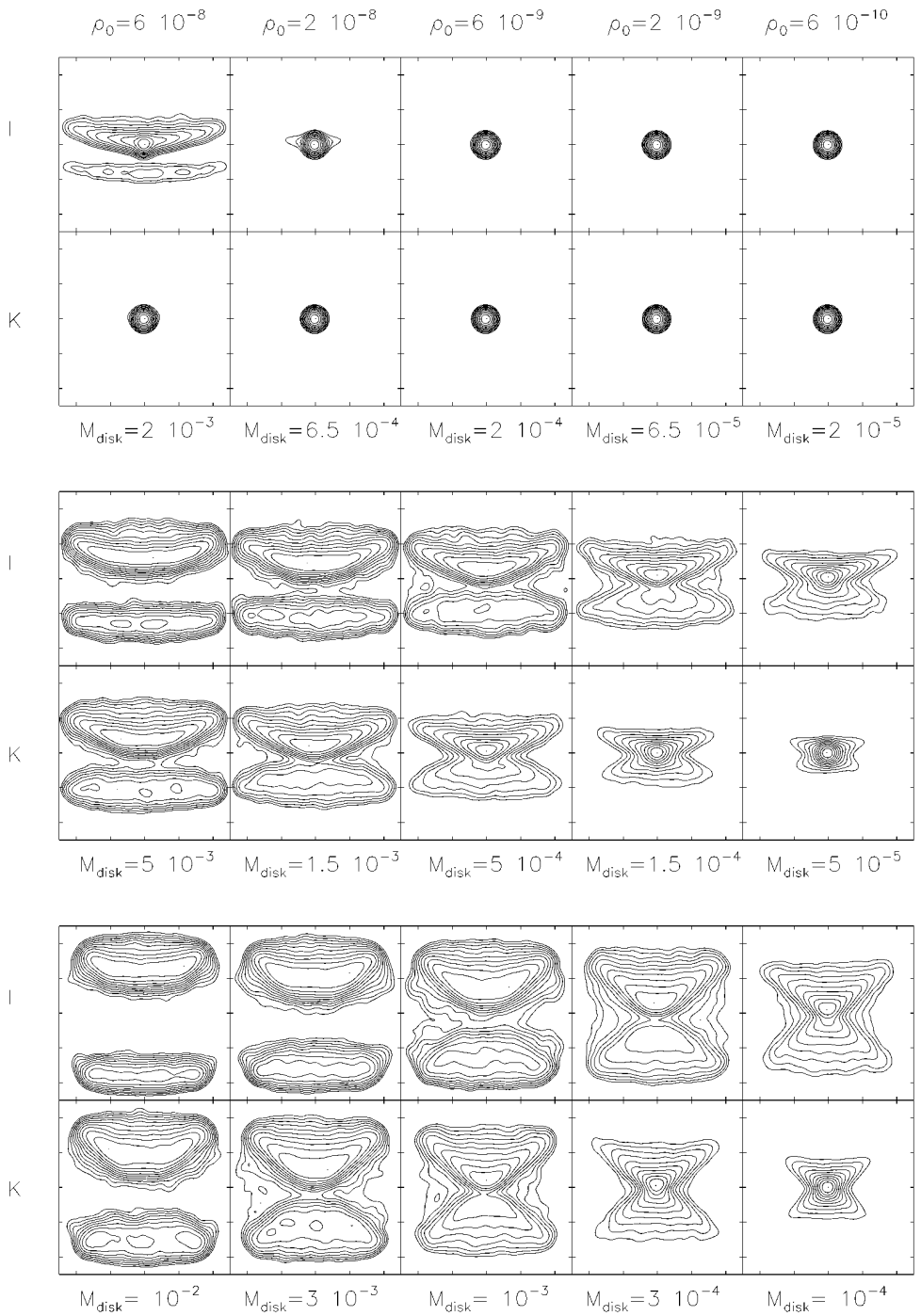

FIG. 1*a*

FIG. 1.—(*a*) *I*- and *K*-band scattered light images for a disk viewed at an inclination of $i = 82°$ with flaring parameter $\beta = 9/8$ and scale heights at 100 AU of 7 AU (*upper panel*), 15 AU (*middle panel*), and 30 AU (*lower panel*), i.e., $h_0 = 0.02$, 0.05, and $0.1R_*$, respectively. The disk mass varies from 2×10^{-5} to 10^{-2} $M_\odot$ and the density at the stellar surface is in the range 6×10^{-10} g cm^{-3} $\leq \rho_0 \leq 6 \times 10^{-8}$ g cm^{-3}. Each box is 500 AU on a side and the flux contours are at 0.5 mag intervals, with the lowest contour being 1% of the maximum in each plot. Disks with small scale height (7 AU) are undetectable unless they are very massive. As the disk mass is decreased, notice the transition from two separated nebulae, to an hourglass morphology, and then to a single peak in the images. (*b*) Pole-on spectral energy distributions for reprocessing stellar radiation in an optically thick flared disk with $\beta = 9/8$ and scale heights at 100 AU of 7, 15, and 30 AU. Also shown is the calculation for an optically thick flat disk.

Our model *I*- and *K*-band images in Figures 1*a*, 2*a*, and 3*a* show that disks with small scale heights ($\sim$7 AU) are difficult to detect unless they are very massive ($\geq 10^{-2} M_\odot$) or seen almost exactly edge-on (since for such small scale heights there is less of an inclination range where the star is occulted by the disk). As the scale height increases, there is more disk material at high latitudes above the midplane to intercept and scatter the stellar radiation yielding "boxier" images. For a given scale height, decreasing the disk density (i.e., disk mass or optical depth) results in the images progressing from two nebulae separated by the dark dust lane of the disk, to the joining of the two nebulae, and eventually

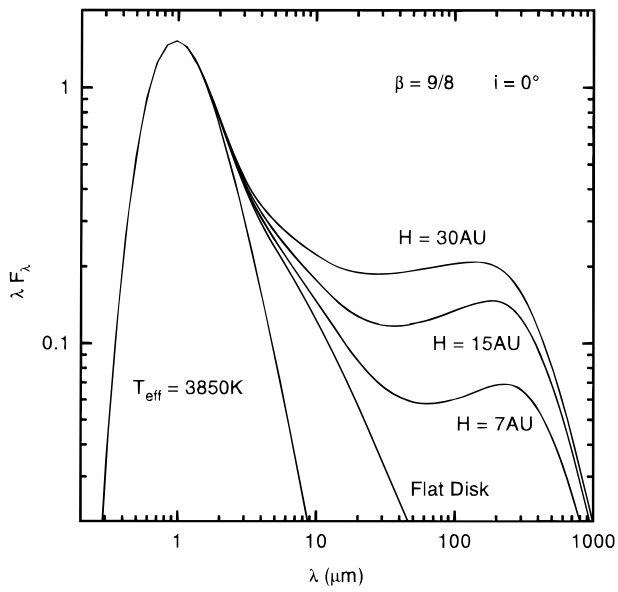

FIG. 1*b*

to a single peak in the flux image. The *K*-band images change from the "hot dog" to the "hourglass" shape more rapidly than the *I*-band images. The lower opacity at *K* relative to *I* yields more diffuse flux.

It is clear from this set of model images that, if the scale height at 100 AU is held fixed (by changing h_0 and β accordingly), the images are fairly insensitive to the degree of flaring. The images are also insensitive to the inner radius of the disk (see Burrows et al. 1996). Close to the star, the disk is geometrically thin, and it is the outer regions, where the flaring and scale height are large, that govern the shape of the images. Thus, from imaging alone and assuming a radial density law, we can estimate the disk scale height at large radii and estimate the disk mass from the optical depth, whose scale is set by $\rho_0 \kappa R_*$, required to match the image (i.e., whether the image is single peaked, or from the width of the separating dust lane in images with two nebulae).

Although the images are rather insensitive to the degree of flaring and the inner disk radius, the spectral energy distributions depend on these parameters. The inner radius sets the level of the near-IR excess; disks with large flaring can intercept more stellar radiation and yield large far-IR excesses (Kenyon & Hartmann 1987). Our pole-on calculations confirm these conclusions for the disk geometries appropriate for our Monte Carlo simulations. For the $\beta = 9/8$ and $\beta = 1.2$ disks, the pole-on IR spectral energy distributions shown in Figures 1*b*, 2*b*, and 3*b* are typical of those observed in classical T Tauri stars. Figure 4 shows a "composite" spectral energy distribution for an M0 T Tauri star ($T_{\rm eff} = 3850$ K), taken from the data presented in Kenyon & Hartmann (1995).

In Figures 1*b*, 2*b*, and 3*b*, we see that as the scale height, h_0, increases, the disk can intercept more stellar radiation, yielding larger IR excesses. There is little excess shortward of 3 μm since we have truncated the disks at an inner radius of $3R_*$. Large excesses shortward of this wavelength would require heating of disk material closer to the star—see, for example, Lada & Adams (1992), Hillenbrand et al. (1992), and Meyer et al. (1997) for the effects of changing the inner radius of the disk. In each of Figures 1*b*, 2*b*, and 3*b*, we have also shown the spectral energy distribution expected from a flat disk with inner and outer radii of $3R_*$ and 250 AU, respectively, using the Adams & Shu (1986) formalism. In the case of the $\beta = 1.5$ disk, we clearly see the effect of the large disk flaring—the flared disk intercepts more stellar radiation at large radii than do the flatter disks. Consequently, this gives a secondary peak in the IR spectral energy distribution at wavelengths longer than ~ 100 μm. Such spectral energy distributions are not observed in classical T Tauri stars (Beckwith et al. 1990; Osterloh & Beckwith 1995; Kenyon & Hartmann 1995), which provides further observational evidence against the disk flaring being larger than $\beta \approx 5/4$. Although these spectral energy distributions have been calculated using approximate formulae, the overall spectral characteristics should prevail with detailed calculations that include scattering and radiative equilibrium in the radiation transfer. Again we stress that these are pole-on calculations where we assume that the dust is optically thick throughout the entire disk, which is unlikely to be true at large radii, therefore yielding an overestimate of the far-IR excess. For inclinations at which the disk occults the central star, more detailed calculations incorporating wavelength dependent opacity and scattering are required to calculate the emergent spectral energy distribution (see, e.g., Efstathiou & Rowan-Robinson 1990, 1991; Sonnhalter, Preibisch, & Yorke 1995).

Having presented images and spectral energy distributions for a selection of model disks, we now focus our attention on the first optical images of an edge-on disk surrounding a T Tauri star.

5. THE CIRCUMSTELLAR ENVIRONMENT OF HH 30

Our present investigation has been motivated by the recent *HST* images and model for the circumstellar environment of HH 30 presented by Burrows et al. (1996). The WFPC2 observations of HH 30, taken in 1994 January and 1995 February, show two bowl-shaped nebulae separated by a dark lane, resembling the scattered light models of edge-on disks by Whitney & Hartmann (1992, 1993) and those in § 4 above. The relative brightnesses and spatial extents of the nebulae changed between the two epochs, suggesting a variable, nonaxisymmetric illuminating source (possibly a spotted star or a binary system) or obscuration by dust clumps or cometary material as proposed for the higher mass Herbig Ae/Be stars (see, e.g., Grinin & Tambovtseva 1995). HH 30 also possesses a highly collimated bipolar jet that extends for 0.1 pc (Mundt, Brugel, & Buhrke 1987; Mundt et al. 1990). This jet is seen in the *V* and *R* *HST* images where the [S II] and [O II] nebular lines are strong in emission. The optical spectrum of HH 30, taken with the Multiple Mirror Telescope (MMT), shown in Figure 5 displays Hα, [O II], and [S II] emission and the Calcium triplet—features that are typical of classical T Tauri stars.

5.1. *Models for the Circumstellar Environment*

When modeling the *HST* images of HH 30, Burrows et al. (1996) used the parameterization of a Keplerian disk given in equation (1). To fit the *HST* images, Burrows et al. allowed the disk inclination, mass, vertical scale height, degree of flaring, radial density exponent, and dust scattering phase function to be free parameters (see Table 3). To match the images, their best disk model flares greatly ($\beta = 1.45$) and has a scale height of 15 AU at a distance of

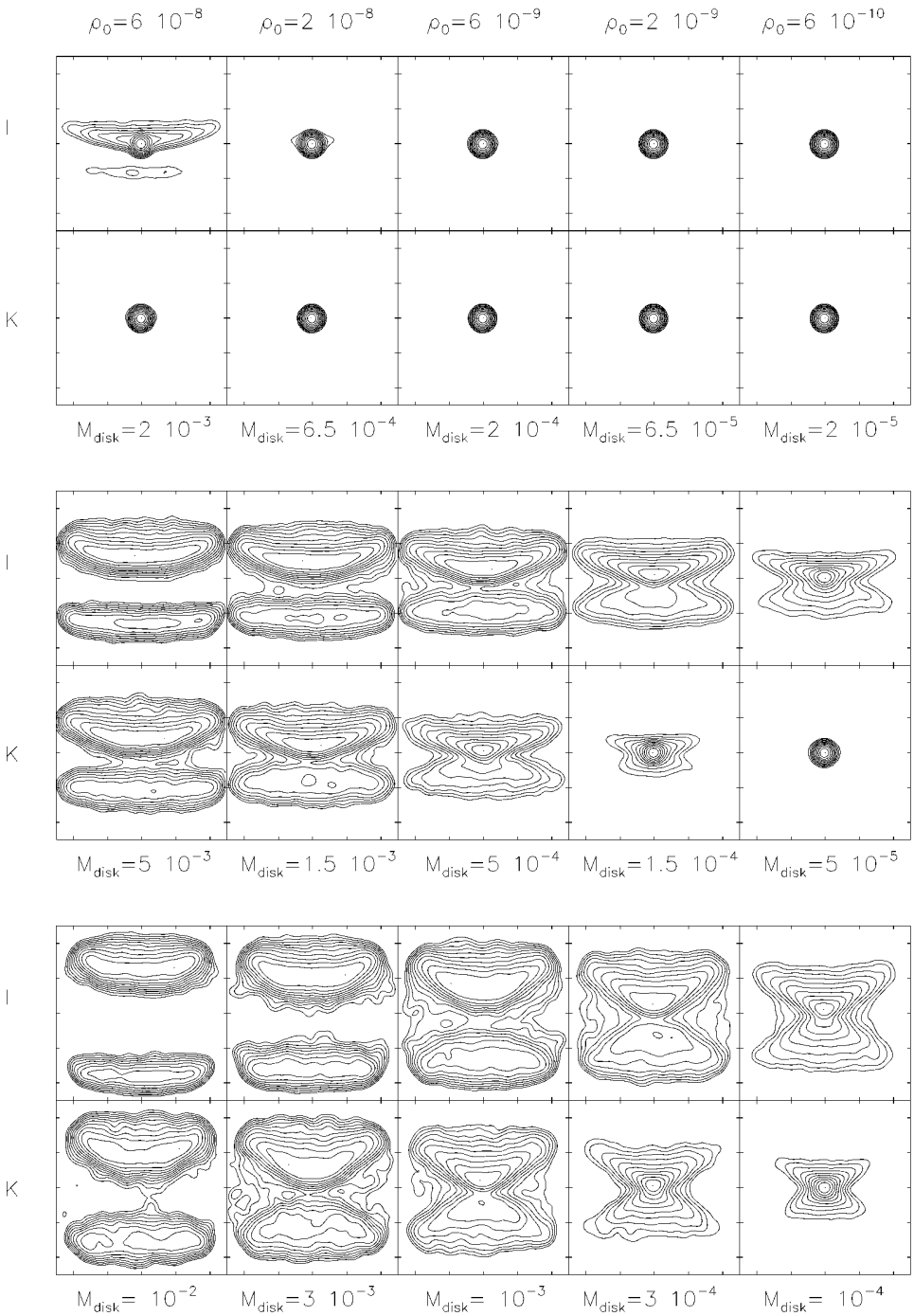

FIG. 2*a*

FIG. 2.—(*a*) As for Fig. 1*a*, but for a flaring parameter of $\beta = 1.2$ and $h_0 = 0.01$, 0.025, and 0.05 R_*. (*b*) As for Fig. 1*b*, but for a disk with flaring parameter $\beta = 1.2$.

100 AU from the central star. This yields a very small scale height at the stellar surface, $h_0 = 0.0025R_*$ for $R_* = 2\ R_\odot$. They also assumed the disk to be dust free from the stellar surface out to a radius of 0.5 AU ($\sim 50R_*$). Although Burrows et al. obtained reasonable fits to the scattered light images, their derived parameters are somewhat extreme. In particular, the large disk flaring is very close to that expected for an isothermal disk ($\beta = 1.5$). Such a high degree of flaring will allow stellar photons to heat the disk at large radii, thereby yielding a very large far-IR excess (as evident in our Fig. 3*a*). In addition, their disk will not produce much near-IR emission, since this requires heating of disk material at distances much closer than the 0.5 AU hole derived in their model fitting procedure. To illustrate these points, we have calculated a model SED using their disk parameters and the Kenyon & Hartmann (1987) semi-analytic approximation for the reprocessing of stellar radiation in a vertically isothermal flared disk. We present this calculation in § 5.1.2 and defer discussion of it until then.

The extreme disk flaring derived by Burrows et al. (1996) appears to mimic a jet-carved cavity within an infalling envelope. This prompted us to investigate whether the *HST*

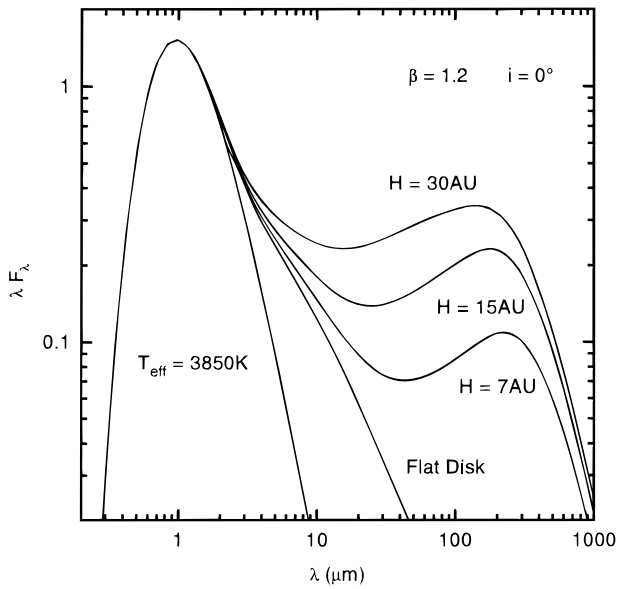

FIG. 2*b*

images of HH 30 could be modeled assuming a circumstellar geometry typical of a class I source (§ 5.1.1). In § 5.1.2, we reexamine the disk hypothesis but keep the parameters controlling the disk geometry within physically and observationally acceptable ranges. Our radiation-transfer models allow us to make high-resolution IR flux and polarization images, which may be compared with forthcoming observations. We have convolved our model images with a Voigt profile with an FWHM of 0.2". This simulated point-spread function is comparable to an *HST* WFPC2 point-spread function calculated with the TINYTIM software (Krist 1995).

HH 30's jet is very prominent in the *V* and *R* *HST* images. We include jet emission in our *R*-band models by releasing jet photons from a cylinder of radius $R_{\rm jet}$ and luminosity $L_{\rm jet}$. The jet luminosity is assumed to fall off as $1/z$ with distance along the jet axis. In our simulations, the jet is a source of unpolarized emission only and contains no dust.

5.1.1. *Class I Source*

The geometry that we adopt for modeling HH 30 as a class I source comprises a large infalling circumstellar envelope and a smaller radius circumstellar disk. The density distribution for the rotating, infalling envelope has been calculated by Terebey et al. (1984), following calculations by Ulrich (1976) and Cassen & Moosman (1981). In these models, particles fall along parabolic orbits toward the central object and stop when they hit the disk. The resulting envelope density is

$$\rho = \frac{\dot{M}}{4\pi}\left(\frac{GM}{r_c^3}\right)^{-1/2}\left(\frac{r}{r_c}\right)^{-3/2}\left(1+\frac{\mu}{\mu_0}\right)^{-1/2}\left(\frac{\mu}{\mu_0}+\frac{2\mu_0^2 r_c}{r}\right)^{-1}, \quad (5)$$

where $\mu = \cos\theta$ and μ_0 is the angle of a particle orbit as $r \rightarrow \infty$. The centrifugal radius, r_c, is the maximum radius at which infalling material hits the midplane and is roughly the outer radius of the disk. The parameters controlling the envelope geometry are the infall rate, $\dot{M}$, and centrifugal radius, r_c, which in turn depends on the rotational velocity, Ω, and outer radius, $R_{\rm max}$. From modeling of many embedded sources in Taurus, Kenyon et al. (1993a, 1993b) and Whitney et al. (1997) found that the observations were best matched with $\dot{M} \approx 3 \times 10^{-6}\ M_\odot\ {\rm yr}^{-1}$ and $r_c \approx 50$ AU for an adopted $R_{\rm max} \approx 10^4$ AU. We adopt these values for HH 30 and set the central mass at $M_* = 0.5\ M_\odot$. The circumstellar disk in our simulations has a density given by equation (1) with $\rho_0 = 2 \times 10^{-7}$ g cm^{-3}, $\alpha = 2$, $\beta = 9/8$, $h_0 = 0.03R_*$, and an outer radius of 50 AU (the centrifugal radius). As explained in Whitney & Hartmann (1993), the dark lane present in our model images in Figure 6 is caused by extinction in the denser equatorial regions of the circumstellar envelope—the small circumstellar disk does not contribute significantly to the extinction above the midplane.

To model the scattered light images of class I sources, Whitney & Hartmann (1993) and Kenyon et al. (1993b) required optically thin routes to allow the stellar photons to escape from the circumstellar envelope. This was achieved by including evacuated cavities in the circumstellar geometry of equation (5). Such cavities are presumably carved by the energetic jets and outflows associated with class I and II sources. The models presented by Whitney & Hartmann (1993) and Kenyon et al. (1993a, 1993b) assumed that the cavity shapes were given by particle streamline trajectories from the Terebey et al. (1984) solution. However, to date few theoretical investigations have been conducted into the expected shape of such cavities (Raga & Cabrit 1993). In the models presented here, we allow the cavities to have a shape according to

$$z_{\rm cav}(\varpi) = z_0 + z_1\left(\frac{\varpi}{R_*}\right)^{\zeta}, \quad (6)$$

where $z_{\rm cav}$ is the shape of the cavity wall above the disk midplane and z_0 sets where the cavity intersects the equatorial plane (if at all). In our simulations, we assume that the cavity intersects the midplane at 0.5 AU from the star and has an exponent $\zeta = 1.5$ and a shape set by the half-opening angle, $\Delta\theta$, defined by

$$\tan\Delta\theta = \frac{R_{\rm max}}{z_{\rm cav}(R_{\rm max})}. \quad (7)$$

The high resolution provided by *HST* should enable us to probe the shapes of cavities in class I sources.

Figure 6 shows the *HST* *R*-band image of HH 30 along with some of our envelope models. In the models, we have included a jet with a total luminosity at *R* of $L_{\rm jet} = 10^{-2}L_*$. The first model shows the scattered light image for the Terebey et al. (1984) density with $R_{\rm max} = 5000$ AU and a cavity opening angle of $\Delta\theta = 30°$. In the second and third

TABLE 3

HH 30 PARAMETERS FROM BURROWS ET AL. (1996)

Parameter	Value
i (deg)	82.5
$M_{\rm disk}$ ($M_\odot$)	4×10^{-4}
H(100 AU) (AU)	15
β	1.45
α	2.23
g	0.64
$R_{\rm in}$ (AU)	0.5
$R_{\rm disk}$ (AU)	250

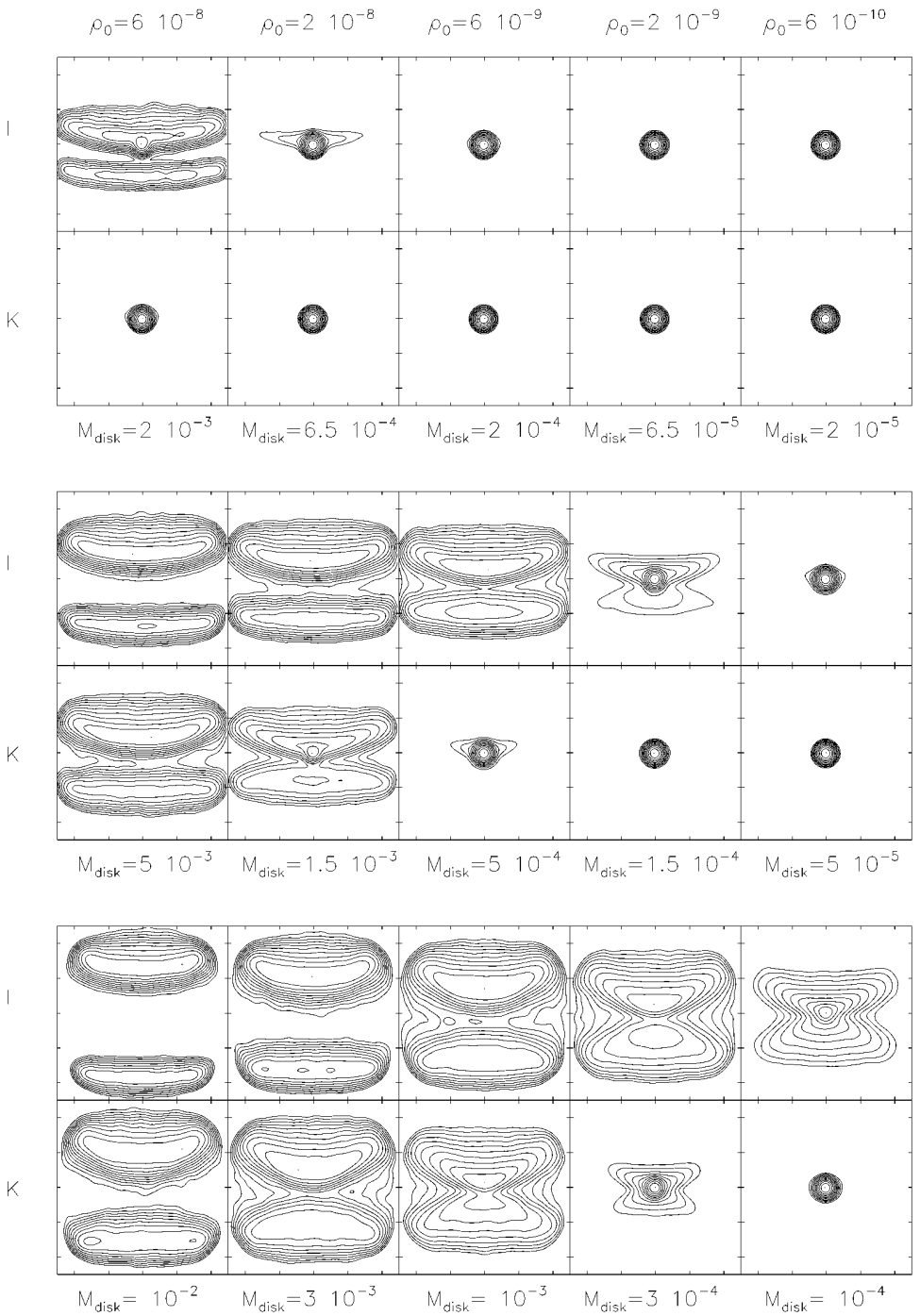

FIG. 3*a*

FIG. 3.—(*a*) As for Fig. 1*a*, but for a flaring parameter of $\beta = 3/2$ and $h_0 = 7 \times 10^{-4}$, 1.5×10^{-3}, and $3 \times 10^{-3} R_*$. (*b*) As for Fig. 1*b*, but for a disk with flaring parameter $\beta = 3/2$. Notice the large far-IR excess due to the large disk flaring that enables the disk to intercept much more stellar radiation at large radii than the flatter disks of Figs. 1 and 2. This excess is overestimated since we use the optically thick flared disk approximation.

models, we have truncated the infalling envelopes at a radius of 500 AU and set the opening angles to be $\Delta\theta = 40°$ and 50°, respectively. While these models are qualitatively similar to the HH 30 data, it is clear that in all cases the models produce images that are at least twice as big as the size of the HH 30 data. From this modeling, we conclude that the circumstellar environment of HH 30 cannot be modeled as a class I source.

5.1.2. *Class II Source*

We now investigate whether HH 30's circumstellar structure can be modeled as a disk with a density distribution given by equation (1). This is the same form for the density as investigated by Burrows et al. (1996). However, in our Monte Carlo simulations, we keep $9/8 \leq \beta \leq 5/4$ and the radius of the inner disk hole fixed at 3 R_* and assume that

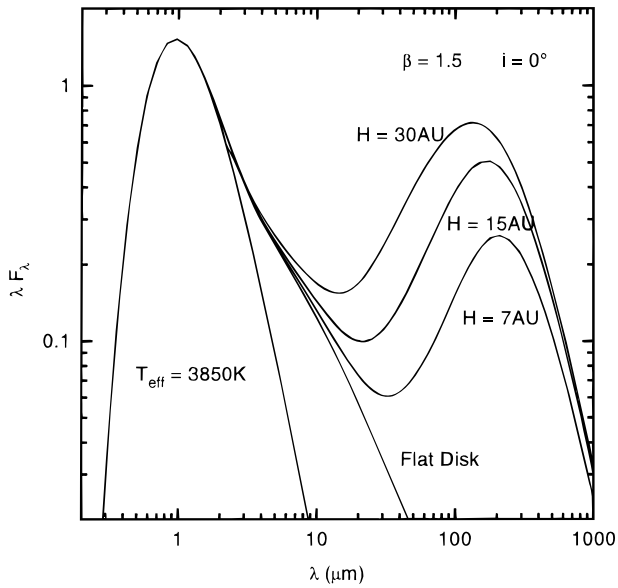

FIG. 3*b*

the dust parameters are those of Table 1. Therefore we keep the parameters within observationally and theoretically plausible limits. We then perform the Monte Carlo radiation-transfer simulations for the *I*-band, varying h_0 and optical depth (whose scale is set by $\rho_0 \kappa R_*$) until we can match the data. For the *R*- and *K*-band simulations, we keep the density structure determined for the *I*-band but change the dust parameters according to wavelength. In addition, for the *R*-band we include luminosity from a bipolar jet.

Unlike Burrows et al. (1996), we have not attempted to perform any kind of least-squares model-fitting procedure. We feel that such a detailed procedure is not justified since our model consists of uniform illumination of an axisymmetric density structure and the data clearly show departures from axisymmetry with the spatial variation of the

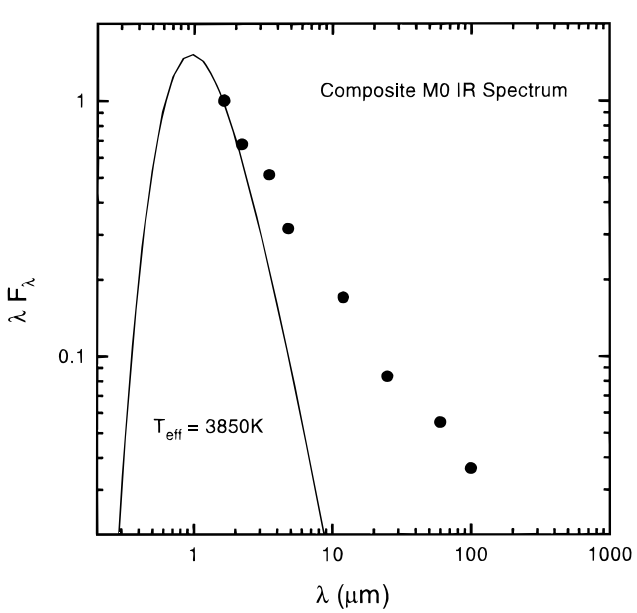

FIG. 4.—Composite IR spectrum for an M0 star taken from Kenyon & Hartmann (1995). Also plotted is the Planck function for $T_{\rm eff} = 3850$ K with the M0 spectrum normalized to the Planck function at *H*.

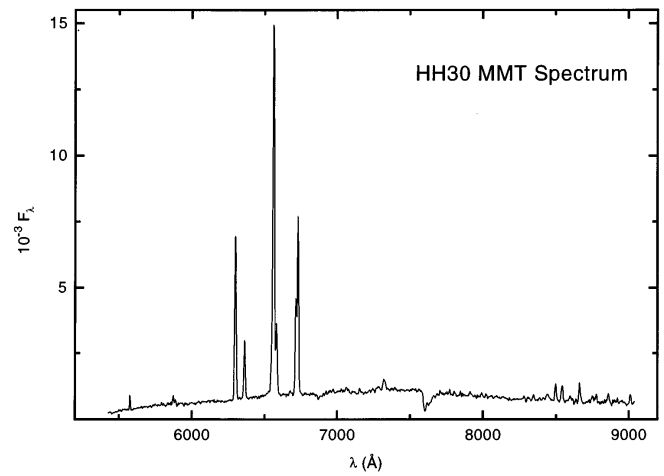

FIG. 5.—Optical MMT spectrum of HH 30. The Hα, [O II], [S II], and the Calcium triplet are typical of classical T Tauri stars.

scattered light. Burrows et al. also noted that the two scattered light nebulae changed in brightness by different amounts and in opposite directions between the two *HST* observations they reported. Whether these changes are caused by a variable source (e.g. star spots) or occultation by circumstellar material is unclear at present. Until further studies into the variability of HH 30 are performed, we restrict our modeling efforts to determining the gross properties of the circumstellar environment.

Figure 7 presents the *R*- and *I*-band *HST* data on HH 30, our model simulations, and *K*-band predictions. We have also performed simulations for the parameters determined by Burrows et al. (1996). In the case of the Burrows et al. simulations, we use their derived *I*-band parameters (Table 3) for the *I*-band simulation. For the *R* and *K* simulations, we use their density, scale height, flaring, and inner disk radius, but we use the dust parameters from our Table 1. We also show vertical cuts through the *I*-band data and models in Figure 8. For the cuts through the *HST* data, we have averaged over a vertical strip 3 pixels wide ($\sim$45 AU). The cuts through our model simulations have also been averaged over a strip of the same width.

Figure 7 shows that our *R*- and *I*-band simulations closely resemble the *HST* data. As we discussed in § 4, the images are fairly insensitive to the degree of flaring, provided that the scale height is held fixed at 100 AU. The *R*-band images include a jet of luminosity $L_{\rm jet} = 5 \times 10^{-3} L_*$. The lower jet is stronger in our simulations than in the *HST* data. This is likely to be a result of our adoption of a smooth jet, when in reality the jet possesses many knots ejected from the central source. In the *I*-band simulations, the lower nebula in the Burrows et al. (1996) image is smaller than in our simulations. This is because of the large forward-throwing phase function derived by Burrows et al. It is certainly possible that the circumstellar grains are more forward throwing than we have modeled, but since changing our adopted dust parameters would introduce many more variables into the model fitting, we have kept the parameters in Table 1 fixed. In any case, the smaller lower nebula could be produced by nonaxisymmetric illumination by the star or jet without appealing to dust parameters. The *K*-band simulations show the same trends present in Figures 1*a*, 2*a*, and 3*a*, with a much smaller scattered light nebulae. At *K*, the Burrows et al. (1996) geometry will

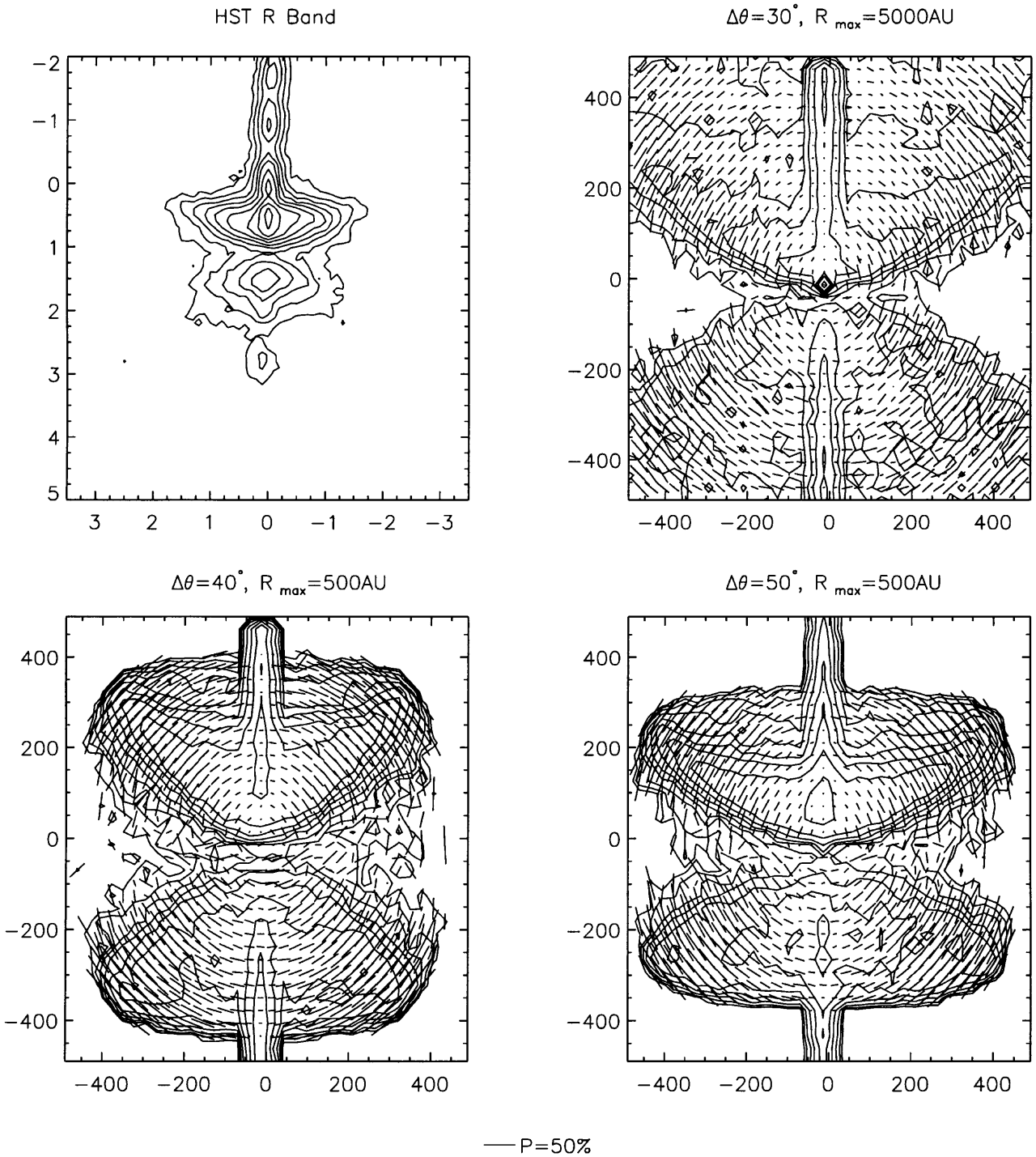

FIG. 6.—*R*-band *HST* image of HH 30 and *R*-band envelope models. The axes for the *HST* image are labeled in arcsec offsets and the model axes are labeled in AU. The model and data are on the same scale, assuming HH 30 is at 140 pc. Contour levels are in 0.5 mag intervals with the lowest contour at 2% of the peak flux in each image. All models are too extended when compared with the *HST* data, leading us to rule out the possibility that HH 30 is a class I source.

produce a point source, as a result of the combination of the more diffuse density structure and the lower *K*-band opacity and albedo. The polarization for all simulations is perpendicular to the disk and displays similar patterns to those predicted by Whitney & Hartmann (1992).

Figure 8 shows a calculation for the "pole-on" spectral energy distributions for the disk models presented in Figure 7. Since the spectral type of HH 30 is unknown, we assume a type of M0, $T_{\rm eff}$ = 3850 K, which is typical of classical T Tauri stars in Taurus (Kenyon & Hartmann 1995). For the Burrows et al. (1996) disk, there is no near-IR excess radiation because of the large dust-free inner region, and the large flaring (β = 1.45) yields a very large far-IR excess, similar to the calculations presented in § 4. Assuming HH 30 is a class II T Tauri star, if it was viewed pole-on, we would expect to see a near-IR excess and a spectral energy distribution that declines toward longer wavelengths (cf. Fig. 4). Neither of these features are present for the calcu-

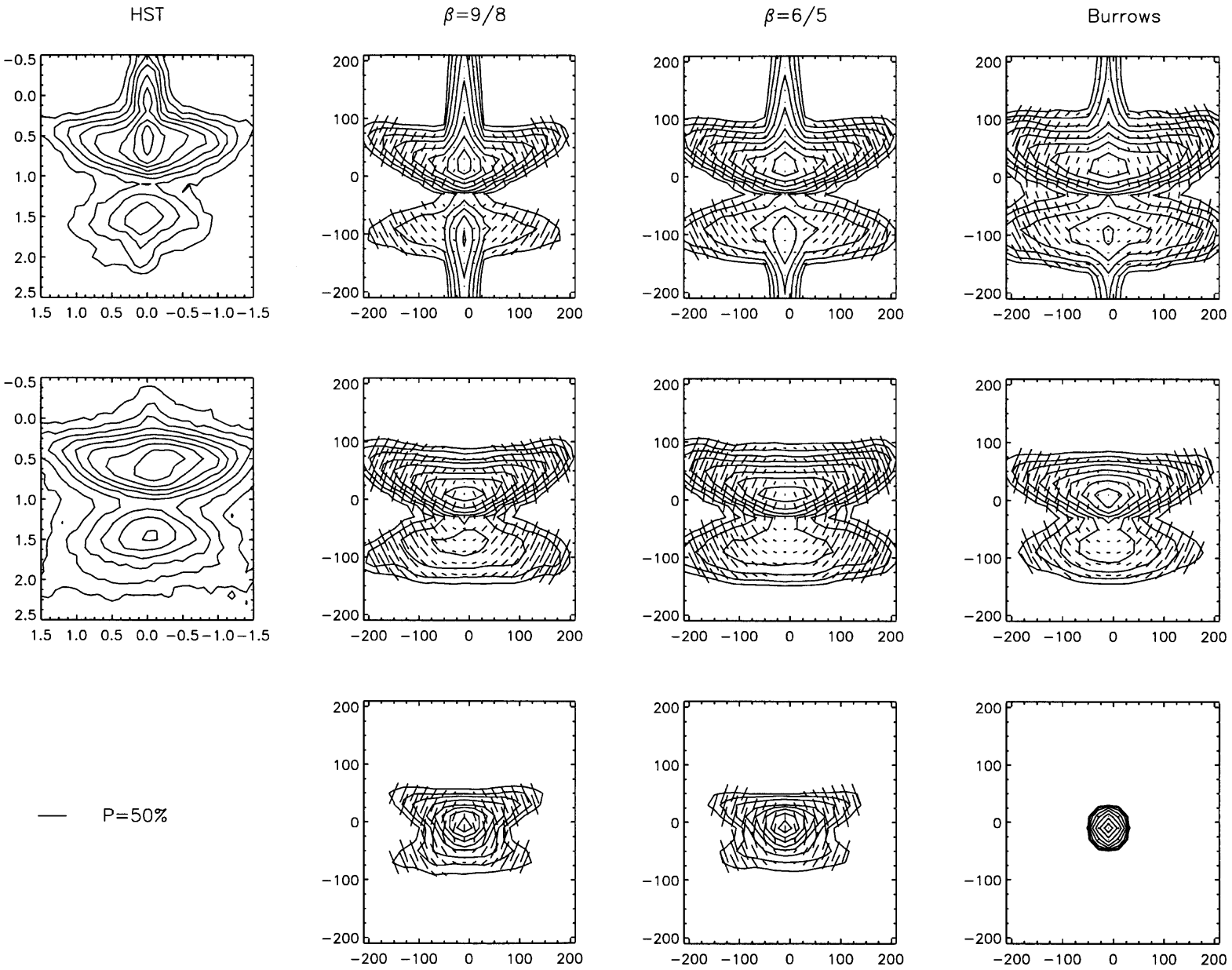

FIG. 7.—*R*- and *I*-band *HST* images of HH 30 and *R*-, *I*-, and *K*-band disk models. Axes are in arcsec for the data and AU for the models and are scaled to be the same size on the sky assuming a distance to Taurus of 140 pc. We show disks with flaring of $\beta = 9/8$ and 1.2; we also show simulations using the parameters derived by Burrows et al. (1996) The Burrows et al. structure predicts a point source at *K*.

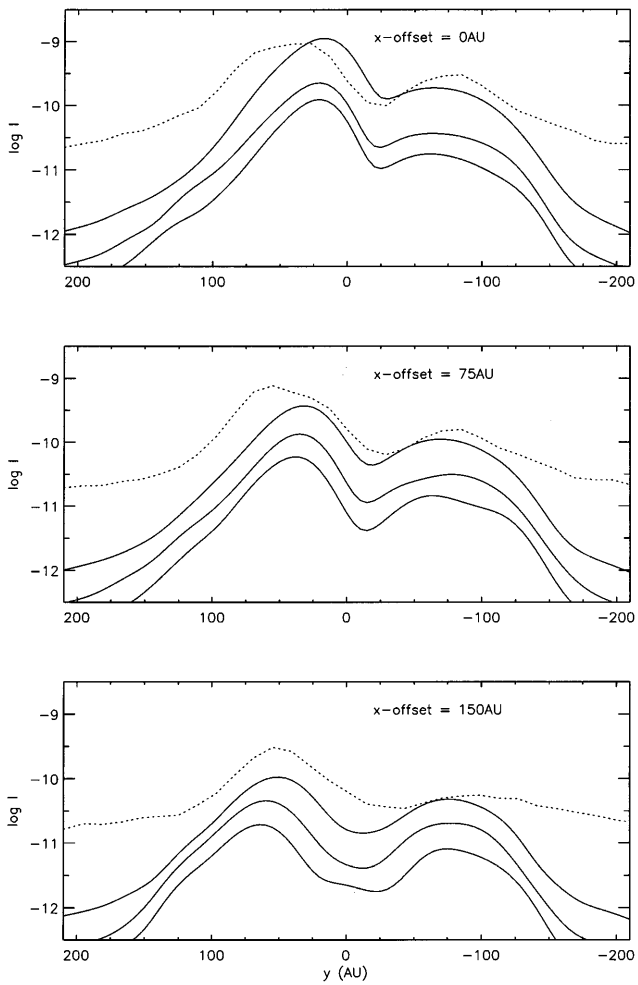

FIG. 8.—Vertical cuts through the *I*-band *HST* data and *I*-band disk models. The dotted curve is the *HST* data and the solid lines are the models. The Burrows et al. (1996) model is the upper of the three solid lines followed by the $\beta = 6/5$ and then the $\beta = 9/8$ models. Note the similarity in the morphologies of the disk models, and that the data is brighter than the models by over an order of magnitude at large distances from the peak intensity, presumably because of scattering off remnant envelope material not present in our disk models.

lation using the parameters derived by Burrows et al. (1996), suggesting that their fit is somewhat extreme. In contrast, the less extreme flaring disks with $\beta = 9/8$ and $\beta = 1.2$ produce spectral energy distributions that are more typical of classical T Tauri stars, but an accurate determination of the far-IR excess requires a detailed radiation-transfer calculation.

A further potential test of the geometry is from polarization measurements. Unresolved, broadband (4600–7000 Å) polarization measurements of HH 30 (Cohen & Schmidt 1981) yield a net polarization of 2.8% at an angle of 60° to the disk rotation axis. Disk models predict polarizations that are parallel to the rotation axis (i.e., perpendicular to the disk midplane). If there is enough scattering material above the disk midplane, it is possible to obtain a polarization position angle that is flipped by 90° to those obtained with our disk models in Figure 7, yielding a polarization position angle *parallel* to the disk (i.e., perpendicular to the disk rotation axis). This situation occurs in infalling envelope models or in very dense disks viewed edge-on (see, e.g., Whitney & Hartmann 1992, 1993). The polarization measurements of Cohen & Schmidt (1981) seem to indicate the presence of high-latitude material. However, the fact that their measured polarization position angle lies at 60° to the disk rotation axis makes this somewhat inconclusive, since all axisymmetric models (whether disks or envelopes) predict a net polarization that is either parallel or perpendicular to the rotation axis.

Taking vertical cuts through the models and data yields stronger evidence for the presence of high-latitude material. The vertical cuts through the *I*-band data and models are shown in Figure 9. The 45 AU wide cuts are taken through the center of the images and at offsets of 75 AU and 100 AU, respectively. The intensity scale is not important since the intrinsic luminosity of the source is unknown and, as with the images in Figure 7, it is the overall shape of the intensity that we are comparing. The models, which are all very similar in shape, resemble the data in the separation and strengths of the two peaks of the scattered light nebulae. However, at large y distances from the center of the cuts, the data are brighter than the models by at least an order of magnitude. This may be because of light scattering off remnant material from an infalling envelope that is not included in our class II density structure. This extra light drove Burrows et al. (1996) to derive a more flared model. The Gaussian vertical structure of the disk results in very little disk material after a couple of scale heights above the midplane that does not match the data.

We have attempted to reduce the discrepancy between the *I*-band data and models by introducing an optically thin envelope in addition to the disk. As in § 5.1.1, we use the Terebey et al. (1984) infalling envelope geometry with bipolar cavities. Since Figure 9 indicates that any circumstellar envelope is rather diffuse, we use a much smaller infall rate. Figure 10*a* shows an *I*-band model, and in Figure 10*b* we show the vertical cuts through the data and model. This model consists of a star plus disk ($M_{\rm disk} = 2.5 \times 10^{-4}\ M_\odot$, $\beta = 9/8$, $H(100\ {\rm AU}) = 15$ AU) and a Terebey et al. (1984) infalling envelope ($R_{\rm max} = 1000$ AU, $R_c = 250$ AU, $\dot{M} = 3 \times 10^{-8}\ M_\odot\ {\rm yr}^{-1}$, $\Delta\theta = 20°$). This geometry

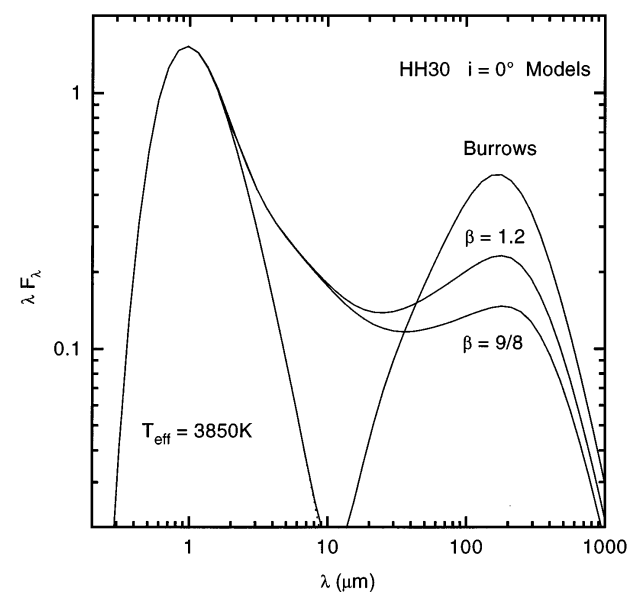

FIG. 9.—Pole-on spectral energy distribution calculations for the HH 30 disk models. Notice the lack of near-IR excess (caused by the 0.5 AU inner disk hole) for the Burrows et al. (1996) geometry. The far-IR excess is overestimated because of the optically thick approximation adopted.

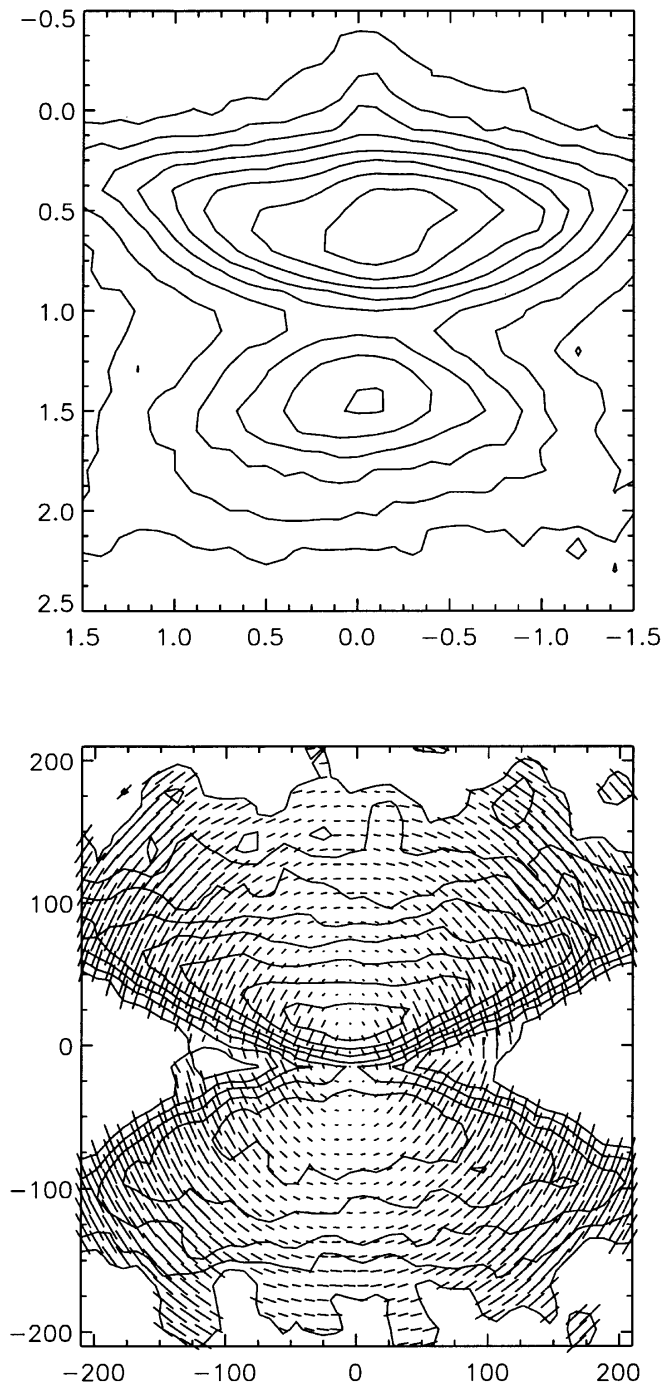

FIG. 10*a*

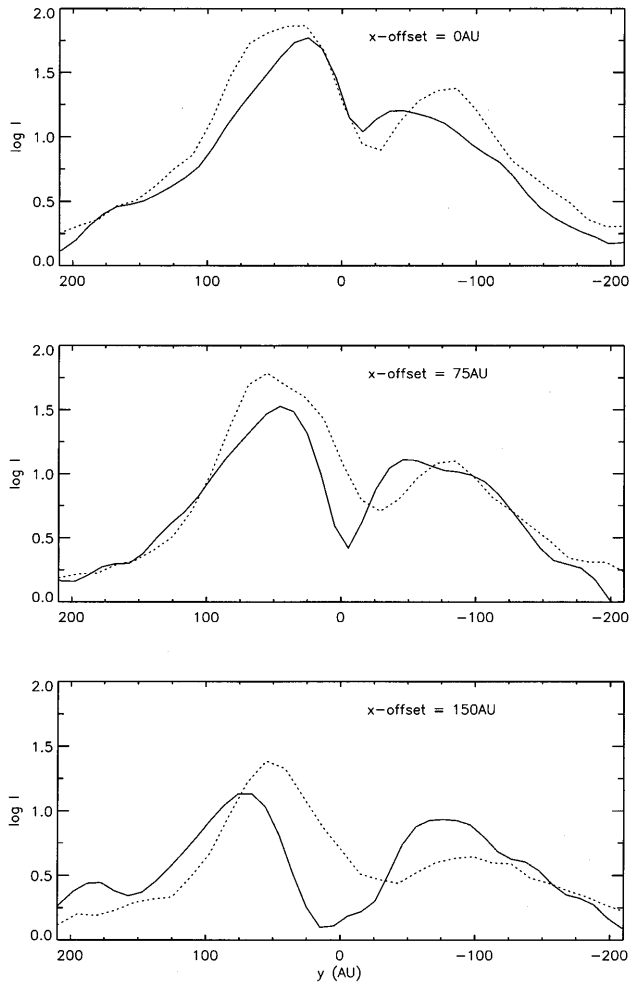

FIG. 10*b*

FIG. 10.—(*a*) *HST I*-band image of HH 30 (*upper panel*). Model scattered light image consisting of a central star, circumstellar disk, and an optically thin infalling envelope (*lower panel*). Axes are in arcsec for the data and in AU for the model and are scaled to be the same size on the sky. (*b*) Vertical cuts through the *I*-band *HST* image (*dotted lines*) and through the disk plus infalling envelope model (*solid lines*) of Fig. 10*a*.

gives a better match to the scattered light at high latitudes than the disk-only models. However, the net polarization is still perpendicular to the disk (parallel to the disk rotation axis). The models presented in Figure 10 show that some diffuse infalling envelope is required to match the data. High-resolution imaging polarimetry will help in further constraining the circumstellar mass and geometry.

We conclude that the scale height of HH 30's disk is about 15 AU at a distance of 100 AU from the star—as also found by Burrows et al. (1996). The optical depth required to produce the observed dust lane implies a total disk mass of around $2.5 \times 10^{-4}\ M_{\odot}$. The inclination of the system is around 80°, in agreement with the determination by Burrows et al. We cannot yet ascertain the degree of flaring of the disk from the optical images. Disks with $9/8 \leq \beta \leq 3/2$ yield reasonable optical images. The *K*-band images of these disks vary considerably (Fig. 7) and provide a means to distinguish between models. Spectral energy distribution

calculations also place limits on disk flaring, with our pole-on approximations in Figure 9 showing the effect of increasing the disk flaring. Smaller β disks are favored if HH 30 is a typical classical T Tauri star.

From 1.3 mm continuum observations, Osterloh & Beckwith (1995) find that disk masses are typically in the range 0.01–0.1 $M_{\odot}$. It is unclear how to compare masses derived from radio data with those derived from optical scattered light images. Scattered light modeling probes structures close to the star, while analysis of millimeter-continuum data allows one to sample extended low-density dust and to obtain an estimate of the radial density variation (our α). Combining the millimeter data with the scattered light models may help to resolve the degeneracy arising from the choices of α and β in the scattered light imaging (Burrows et al. 1996). Accurate calculations of the radial and vertical temperature structure of the disk are crucial for estimating the radio flux. Such a temperature calculation requires accurate radiative equilibrium calculations accounting for the scattering, absorption, and reemission of stellar and accretion luminosity within the disk. Such studies are time consuming and have been limited in the range of disk masses investigated (see, e.g., Efstathiou & Rowan-Robinson 1990, 1991; Sonnhalteret al. 1995). Clearly, more thorough investigations are required so that we may model the entire spectral energy distribution with a consistent model. The rather low disk mass associated with HH 30 (as determined by this work and also by Burrows et al. 1996) implies that HH 30 is an evolved system. However, the presence of high-latitude material (Fig. 10) and strong outflows are usually associated with very young objects (see, e.g., Gomez et al. 1998). Statistically, around 10% of class II sources exhibit strong outflows (Gomez et al. 1998), so HH 30 may be such an object. Alternatively, since HH 30 is located in a very crowded field of young stellar objects, it is possible that its natal cloud was tidally truncated, leaving a smaller initial mass from which to form the disk. Assuming that HH 30 is of a similar age to the other objects in this field (e.g., HL Tau) would explain the presence of the strong outflows and the high-latitude material. A low initial envelope mass would yield a small extinction through the envelope, enabling us to view the circumstellar disk.

6. DISCUSSION

This paper has investigated the optical and near-IR images and spectral energy distributions that may be observed from classical T Tauri stars—the class II star-plus-disk systems. We have investigated a range of disks with parameters within reasonable theoretical and observational bounds. The results of this investigation have been applied to the circumstellar environment of HH 30. We now give a summary of our findings.

6.1. *Some General Comments on Disks*

Our models illustrate observable features for disks around edge-on T Tauri stars. We have chosen disk parameters (size, mass, shape) that lie within physically plausible limits. Recent papers have attempted to model the circumstellar environment of some T Tauri stars with "disks" with large opening angles (Men'shchikov & Henning 1997). Also, polarization patterns have been attributed to very large disk structures with radii of thousands of AU (see, e.g., Gledhill & Scarrott 1989; Draper, Warren-Smith, & Scarrott 1985; Ward-Thompson, Warren-Smith, & Scarrott 1985). In both of these cases, more plausible models in which the circumstellar environment is that of a class I infalling envelope with jet-carved cavities seem appropriate (Whitney et al. 1997, Lucas & Roche 1997).

As shown by Whitney & Hartmann (1992), since the disks we are modeling are geometrically thin compared to the envelope models, they will be visible only at high inclinations where the disk occults the central star. We find that the model images are fairly insensitive to the degree of disk flaring (exponent β), provided we set the scale height at large radii (i.e., as we increase β we must compensate by decreasing h_0). However, the pole-on spectral energy distribution is sensitive to the disk flaring. Flaring in excess of $\beta \approx 5/4$ yields very large far-IR excesses, which are not observed in classical T Tauri stars. This was noted by Kenyon & Hartmann (1987). The model images are insensitive to the inner radius of the disk, but the spectral energy distribution is sensitive to this radius, since hot disk material close to the star provides most of the observed near-IR excess radiation. Modeling the scattered light images of disks will thus enable us to estimate the disk radius and the scale height at large distances from the central source ($\sim$100 AU) and to obtain an estimate of the disk mass from the optical depth required to give the observed dust lane. In our simulations, we have adopted dust parameters appropriate for the interstellar medium. These dust parameters appear to match the observed extinction and scattered light patterns in T Tauri stars (Whitney et al. 1997). While some features of the scattered light patterns seen in current data may be caused by the dust parameters being different from what we have used, there are many other effects that could cause these patterns—for example, nonuniform illumination and nonaxisymmetric circumstellar densities. As more higher resolution scattered light images become available, more detailed investigations into the circumstellar dust properties will be possible.

6.2. *HH 30*

The scattered light nebulae associated with HH 30 are the first direct optical images of a disk surrounding a class II T Tauri star (Burrows et al. 1996). The model for the disk presented by Burrows et al. is somewhat extreme in that the large flaring ($\beta = 1.45$) will yield a very large far-IR excess and the large inner disk hole (0.5 AU) results in no near-IR excess. This is borne out in our pole-on spectral energy distribution calculations. We investigated whether the HH 30 images could be modeled with a class I density structure, but find that this yields scattered light images that are too large. The disk scenario does appear to be the correct interpretation, but we have been able to successfully model the images with parameters that are more typical for class II sources. Burrows et al. (1996) found that the scale height at 100 AU was around 15 AU. We can reproduce the images adopting this scale height but with less extreme flaring, thereby yielding a reasonable far-IR spectral energy distribution. We also used an inner disk radius of $3R_*$ in accordance with magnetospheric accretion models and this allows for a near-IR excess that is absent in the Burrows et al. (1996) model. The disk mass required to produce the observed dust lane was found to be $2.5 \times 10^{-4}\ M_{\odot}$.

We have been able to match the I-band images by including a diffuse infalling envelope. This provides high-latitude material resulting in an extended vertical scattered light

structure that is absent from models with only a disk. The presence of this material and the strong outflows associated with HH 30 imply it is younger than would be thought for an object with an evolved, low-mass disk. However, gravitational interactions with other nearby objects could have resulted in a low initial mass from which the disk formed

With the successful imaging of HH 30's disk, the prospects are good for imaging other edge-on T Tauri disks. Candidates would be sources that show far-IR spectral energy distributions typical of class II sources but are very faint in the optical because of extinction of starlight by the edge-on disk. On a theoretical front, future work should be directed to calculating accurate spectral energy distributions for disks viewed at arbitrary inclination, in addition to extensions to general three-dimensional geometries and illuminations.

This work has been funded by the *HST* archival research program and NASA grant NAG 5-3430 from the Long Term Space Astrophysics Research Program. We thank the referee, François Menard, for his constructive comments and for encouraging us to construct the disk plus optically thin envelope models in Figure 10.

REFERENCES

Adams, F. C., Emerson, J. P., & Fuller, G. A. 1990, ApJ, 357, 606
Adams, F. C., Lada, C. J., & Shu, F. H. 1987, ApJ, 312, 788
Adams, F. C., & Shu, F. H. 1986, ApJ, 308, 836
Bally, J., Devine, D., Fesen, R. A., & Lane, A. P. 1995, ApJ, 454, 345
Beckwith, S. V. W., Sargent, A. I., Chini, R. S., & Gusten, R. 1990, AJ, 99, 924
Bertout, C., Basri, G., & Bouvier, J. 1988, ApJ, 330, 350
Bouvier, J., & Bertout, C. 1989, A&A, 211, 99
Bouvier, J., Cabrit, S., Fernandez, M., Martin, E. L., & Matthews, J. M. 1993, A&A, 272, 176
Burrows, C. J., et al. 1996, ApJ, 473, 437
Cassen, P., & Moosman, A. 1981, Icarus, 48, 353
Chandler, C. J., Koerner, D. W., Sargent, A. I., & Woods, D. O. S. 1995, ApJ, 449, L139
Close, L. M., Roddier, F., Northcott, M. J., Roddier, C., & Graves, J. E. 1997, ApJ, 478, 766
Cohen, M., & Kuhi, L. V. 1979, ApJS, 41, 743
Cohen, M., & Schmidt, G. D. 1981, AJ, 86, 1228
D'Alessio, P., Calvet, N., & Hartmann, L. 1997, ApJ, 474, 397
Draper, P. W., Warren-Smith, R. F., & Scarrott, S. M. 1985, MNRAS, 216, 7p
Dutrey, A., Guilloteau, S., Duvret, G., Prato, L., Simon, M., Schuster, K., & Menard, F. 1996, A&A, 309, 493
Edwards, S., et al. 1993, AJ, 106, 372
Efstathiou, A., & Rowan-Robinson, M. 1990, MNRAS, 245, 275
———. 1991, MNRAS, 252, 528
Fischer, O., Henning, T., & Yorke, H. W. 1994, A&A, 284, 187
———. 1996, A&A, 308, 863
Ghosh, P., & Lamb, F. K. 1979a, ApJ, 232, 259
———. 1979b, ApJ, 234, 296
Gledhill, T. M., & Scarrott, S. M. 1989, MNRAS, 236, 139
Gomez, M., Whitney, B. A., & Kenyon, S. J. 1997, AJ, 114, 1138
Grinin, V. P., & Tambovtseva, L. V. 1995, A&A, 293, 396
Henyey, L. G., & Greenstein, J. L. 1941, ApJ, 93, 70
Herbst, W., Herbst, D. K., & Grossman, E. J. 1994, AJ, 108, 1906
Hillenbrand, L. A., Strom, S. E., Vrba, F. J., & Keene, J. 1992, ApJ, 397, 613
Kenyon, S. J., Calvet, N., & Hartmann, L. 1993a, ApJ, 414, 676
Kenyon, S. J., & Hartmann, L. 1987, ApJ, 323, 714
———. 1995, ApJS, 101, 117
Kenyon, S. J., Whitney, B. A., Gomez, M., & Hartmann, L. 1993b, ApJ, 414, 773
Kenyon, S. J., Yi, I., & Hartmann, L. 1996, ApJ, 462, 439
Kim, S. H., Martin, P. G., & Hendry, P. D. 1994, ApJ, 422, 164
Konigl, A. 1991, ApJ, 370, L39
Krist, J. E. 1995, in ASP Conf. Proc. 77, Astronomical Data Analysis Software and Systems IV, ed. R. A. Shaw, H. E. Payne, & J. M. E. Hayes (San Francisco: ASP), 349
Lada, C. J. 1987, in Star Forming Regions, ed. M. Peimbert & J. Jugaka (Dordrecht: Kluwer), 1
Lada, C. J., & Adams, F. C. 1992, ApJ, 393, 278
Lucas, P. W., & Roche, P. F. 1997, MNRAS, 286, 895
Lynden-Bell, D., & Pringle, J. E. 1974, MNRAS, 168, 603
Mahdavi, A., & Kenyon, S. J. 1998, ApJ, 497, 342
Meyer, M. R., Calvet, N., & Hillenbrand, L. A. 1997, AJ, 114, 288
Mundt, R., Brugel, E. W., & Buhrke, T. 1987, ApJ, 319, 275
Mundt, R., Ray, T. P., Buhrke, T., Raga, A. C., & Solf, J. 1990, A&A, 232, 37
Men'shchikov, A. B., & Henning, T. 1997, A&A, 318, 879
Osterloh, M., & Beckwith, S. V. W. 1995, ApJ, 439, 288
Ostriker, E. C., & Shu, F. H. 1995, ApJ, 447, 813
Raga, A., & Cabrit, S. 1993, A&A, 278, 267
Shakura, N. I., & Sunyaev, R. A. 1973, A&A, 24, 337
Shu, F. H. 1977, ApJ, 214, 488
Shu, F. H., Adams, F. C., & Lizano, S. 1987, ARA&A, 25, 23
Sonnhalter, C., Preibisch, T., & Yorke, H. W. 1995, A&A, 299, 545
Stapelfeldt, K. R., et al. 1995, ApJ, 449, 888
Terebey, S., Shu, F. H., & Cassen, P. 1984, ApJ, 286, 529
Ulrich, R. K. 1976, ApJ, 210, 377
Ward-Thompson, D., Warren-Smith, R. F., & Scarrott, S. M. 1985, MNRAS, 215, 537
Whitney, B. A., & Hartmann, L. 1992, ApJ, 395, 529
———. 1993, ApJ, 402, 605
Whitney, B. A., Kenyon, S. J., & Gomez, M. 1997, ApJ, 485, 703
Wood, K., Bjorkman, J. E., Whitney, B. A., & Code, A. D. 1996a, ApJ, 461, 847
———. 1996b, ApJ, 461, 828
Wood, K., Kenyon, S. J., Whitney, B. A., & Bjorkman, J. E. 1996c, ApJ, 458, L89